Journal of Inorganic Biochemistry 206 (2020) 110997

Contents lists available at ScienceDirect

Journal of Inorganic Biochemistry

journal homepage: www.elsevier.com/locate/jinorgbio

Hydrolyzed Ce(IV) salts limit sucrose-dependent biofilm formation by *Streptococcus mutans*☆

Lopa Bhatt[a], Lin Chen[b], Jinglong Guo[a], Robert F. Klie[a], Junhe Shi[b], Russell P. Pesavento[c,d,*]

[a] Department of Physics, University of Illinois at Chicago, 801 S. Paulina Street, Chicago, IL 60612, USA
[b] Center for Wound Healing and Tissue Regeneration, College of Dentistry, University of Illinois at Chicago, 801 S. Paulina Street, Chicago, IL 60612, USA
[c] Department of Oral Biology, College of Dentistry, University of Illinois at Chicago, 801 S. Paulina Street, Chicago, IL 60612, USA
[d] The Center for Biomolecular Sciences and Department of Medicinal Chemistry and Pharmacognosy, University of Illinois at Chicago, 801 S. Paulina Street, Chicago, IL 60612, USA

ARTICLE INFO

Keywords:
Ce(IV)
Biofilm
Inhibition
Dental
Streptococcus mutans

ABSTRACT

Several studies have focused on the antimicrobial effects of cerium oxide nanoparticles (CeO_2-NP) but few have focused on their effects on bacteria under initial biofilm formation conditions. *Streptococcus mutans* is a prolific biofilm former contributing to dental caries in the presence of fermentable carbohydrates and is a recognized target for therapeutic intervention. CeO_2-NP derived solely from Ce(IV) salt hydrolysis were found to reduce adherent bacteria by approximately 40% while commercial dispersions of "bare" CeO_2-NP (*e.g.*, 3 nm, 10–20 nm, 30 nm diameter) and $Ce(NO_3)_3{\cdot}6H_2O$ were either inactive or observed to slightly increase biofilm formation under similar *in vitro* conditions. Planktonic growth and dispersal assays support a non-bactericidal mode of biofilm inhibition active in the initial phases of *S. mutans* biofilm production. Human cell proliferation assays suggest only minor effects of hydrolyzed Ce(IV) salts on cellular metabolism at concentrations up to 1 mM Ce, with less observed toxicity compared to equimolar concentrations of $AgNO_3$. The results presented herein have implications in clinical dentistry.

1. Introduction

The composition of clinically relevant biofilms varies significantly depending on the tissue, host and local environment. The oral cavity is home to a diverse array of microorganisms with varying capacities to form biofilms [1]. *Streptococc us mutans* is among the robust tooth-adhering biofilm formers in the presence of fermentable carbohydrates (*e.g.*, sucrose). This increased capacity for biofilm production by *S. mutans* is strongly associated with dental caries [2]. As such, *S. mutans* has long been the target of antimicrobial therapy to limit tooth decay and associated comorbidities [3]. Inorganic tooth-applied agents (*e.g.*, $AgNO_3$, silver diamine fluoride) are effective at arresting tooth decay, yet they are non-selective bactericidal agents whose repeated administration has raised concerns of emerging bacterial resistance [4,5] and deleterious effects on the oral microbiota. Although agents with selective toxicity for highly cariogenic species are welcomed, none are currently available for clinical use. As such, tooth-applied biofilm inhibitors with non-lethal mechanisms of action have defined the search in preventive dentistry with the aim of limiting the effects on the entirety of the oral microbiota.

The use of nanoparticles in preventive and restorative dentistry has received considerable interest in recent years [6,7]. Cerium oxide nanoparticles (CeO_2-NP) are an attractive option for oral application due to their diverse range of sizes and morphologies attributed to variations in synthetic methodology [8]. This morphological diversity may be harnessed into differential medicinal activity [8]. Although the antimicrobial activity of CeO_2-NP has been the subject of several studies and a recent review [9], their effects on biofilm communities have only been reported recently [10–13]. Fewer studies have focused on the interaction of sublethal concentrations of CeO_2-NP with defined bacteria cultures under the initial biofilm formation conditions. Masadeh et al. [14] recently concluded that CeO_2-NP (25–50 nm) were inactive as biofilm inhibitors and they also reduced the activity of known antimicrobial agents against a panel of selected bacteria. Xu et al. reported that CeO_2-NP (50 nm) accelerated *in vitro* biofilm formation in *P. aeruginosa* [15]. It was postulated that bacterial exposure to "bare" CeO_2-

☆ Some of the data presented in this manuscript was published as US 2019/0262393 on August 29, 2019 (U.S. Patent Application No. 16/288,694). This patent application is assigned to the Board of Trustees of the University of Illinois, listing the corresponding author of this manuscript (Russell Pesavento) as the inventor.

* Corresponding author at: Department of Oral Biology, College of Dentistry, University of Illinois at Chicago, 801 S. Paulina Street, Chicago, IL 60612, USA.
E-mail address: rpesaven@uic.edu (R.P. Pesavento).

https://doi.org/10.1016/j.jinorgbio.2020.110997
Received 5 August 2019; Received in revised form 9 January 2020; Accepted 10 January 2020
Available online 11 January 2020
0162-0134/

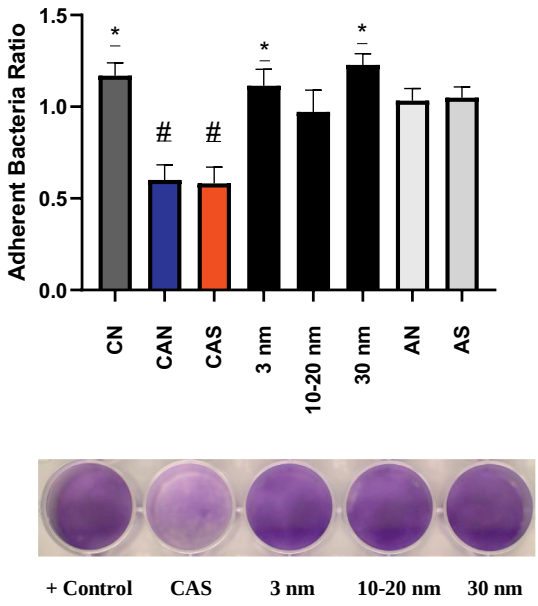

Fig. 1. The ratio of adherent bacteria (compared to positive control) from the treatment of *S. mutans* UA159 with Ce-containing agents (125 μM Ce) [CN = Ce $(NO_3)_3{\cdot}6H_2O$] and ammonium salts (AN, AS) (1 mM) BHI, 1% sucrose, 37 °C, 5% CO_2 for 20 h. $^{*}p < 0.05$, $^{\#}p < 0.0001$, Student *t*-test. The purple stained wells below are indicative of varying levels of adherent bacteria.

NP of this size increased cell surface hydrophobicity, aggregation and the production of reactive oxygen species (ROS) potentiating quorum sensing pathways and enhancing biofilm production [15,16]. The goal of the present study was to expand upon the literature regarding CeO_2-NP as a biofilm inhibiting agent of clinically relevant pathogens. CeO_2-NP prepared from Ce(IV) salt hydrolysis [17–20] were screened against "bare" CeO_2-NP of variable size and $Ce(NO_3)_3{\cdot}6H_2O$ for their ability to perturb initial *in vitro* biofilm formation of the clinically relevant pathogen, *S. mutans*. The aggregation and dispersion properties of similarly sized CeO_2-NP obtained from different synthetic methodology were also investigated offering insight into the variable biological activity observed.

2. Results and discussion

2.1. In vitro adherent bacteria assays

The initial screen for *S. mutans* biofilm inhibition was carried out utilizing 125 μM Ce-containing agents of varying properties on a polystyrene (PS) plate (*See* Fig. 1). All Ce-containing solutions were prepared as 5 mM (Ce ion) stock solutions (aged < 30 min) at room temperature (rt) for consistency and diluted to 125 μM in brain heart infusion (BHI) media containing cells (and 1% sucrose) grown to mid log phase. It should be noted that no statistical difference in inhibitory activity was found when hydrolyzed Ce(IV) salts were allowed to age 20 h (at rt) prior to the static biofilm inhibition assays. Commercial dispersions of "bare" CeO_2-NP: 3 nm solution diameter (Strem, 20% dispersion, pH 3.5 ± 0.75), 10–20 nm solution diameter (Alfa Aesar, 20% dispersion, pH 1.5), 30 nm (Alfa Aesar, 15% dispersion) and $Ce(NO_3)_3{\cdot}6H_2O$ were either inactive or slightly increased biofilm growth of *S. mutans* at 20 h under the above conditions. In contrast, both hydrolyzed CAN (ceric ammonium nitrate) and CAS (ceric ammonium sulfate) displayed a significant reduction in adherent cells (approximately 40%) of *S. mutans* (*See* Fig. 1). Further, dilution of a 1 N solution of $H_2[Ce(NO_3)_6]$ similar to reported methods known to produce CeO_2-NP [17] was found to limit biofilm growth of *S. mutans* comparable to CAN and CAS (data not shown). No inhibition was observed with either 1 mM NH_4NO_3 (AN) or $(NH_4)_2SO_4$ (AS), the byproducts of ceric ammonium salt hydrolysis. The addition of 4 equivalents of AS to stock solutions containing any of the commercially prepared CeO_2-NP (3 nm, 10–20 nm, 30 nm) did not result in increased biofilm inhibition. Further, balancing both the nitrate content and acidity of a CeO_2-NP (3 nm, Strem) dispersion (with 4 M HNO_3) to an equivalent amount present in $H_2[Ce(NO_3)_6]$ did not result in a statistically significant increase in biofilm inhibition at 125 μM (Ce).

2.2. Fluorescence microscopy of adherent biofilm

Light microscopy with fluorescent labeling further supported disruption of *S. mutans* biofilm formation by hydrolyzed Ce(IV) salts. SYPRO™ Ruby Biofilm Matrix Stain (Invitrogen) was used to stain the adherent biofilm post-wash according manufacturers' protocol. Reduction in adherent biofilm was observed in the treated wells (250 μM CAS) as compared to the positive control in Fig. 2.

2.3. Planktonic cellular growth curve analysis

The planktonic growth of *S. mutans* in BHI (37 °C, 5% CO_2) was measured in 30 min intervals in the presence of 500 μM CAN and CAS over 10 h (*See* Fig. 3). Fig. 3 shows that 500 μM CAS had a minimal effect on the planktonic growth of *S. mutans*, while CAN had a lagging effect on the planktonic growth rate that becomes comparable with the positive control over several h. The concentration of CAN and CAS in this assay was 500 μM, approximately *four-fold* the concentration utilized in the initial screening assay in the same growth media (BHI). Thus, the significant reduction in adherent bacteria observed in the initial screening assay (Fig. 1) is attributed to non-bactericidal mechanism(s).

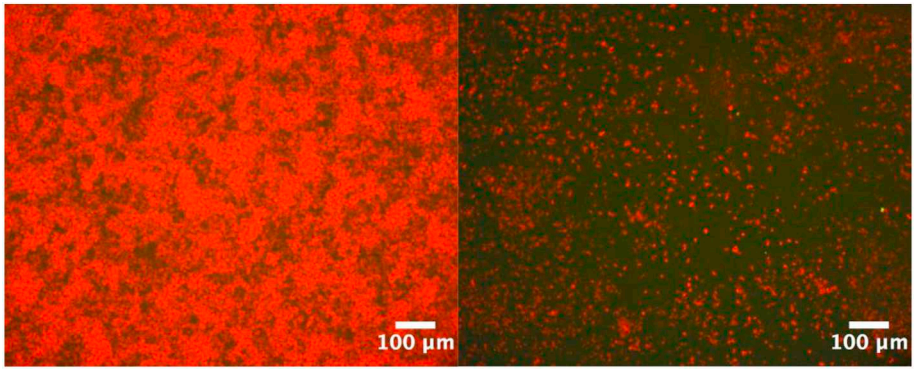

Fig. 2. Microscopic images (10×) of adherent *S. mutans* UA159 grown for 20 h at 37 °C, 5% CO_2 in BHI. The untreated wells (left) displayed significantly more biofilm growth than 250 μM CAS treated wells (right).

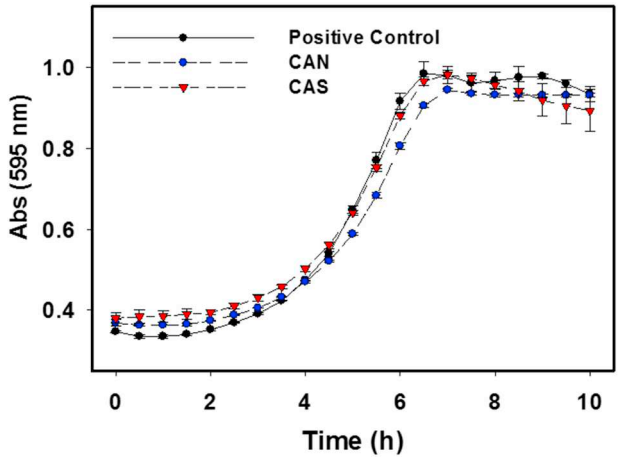

Fig. 3. Planktonic growth curves of *S. mutans* UA159 with 500 μM CAN and CAS treated cells in BHI at 37 °C and 5% CO_2 for 10 h. Measurements were run in triplicate. Error bars represent standard deviation of the triplicate measurements.

2.4. Dose dependent adherent bacteria reduction (IC_{50} determination)

A dose response curve was developed quantifying the effects of varying concentrations (0–1 mM) of CAN on the adherent cells of *S. mutans* grown under similar conditions utilized in the initial screening assay (37 °C, 5% CO_2, 1% sucrose) (*See* Supplemental Data, Fig. S1). The IC_{50} value for reduction in adherent bacteria is 137 μM (± 24 μM) CAN. This demonstrates that the reduction in adherent cells under the initial phase of biofilm growth is directly proportional to the concentration of CAN present.

2.5. Bacterial cell viability assay

The above results prompted further studies on the effects of higher concentrations of hydrolyzed Ce(IV) salts (1 mM) on the planktonic growth of two different and related bacteria that reside in the human oral cavity. *S. mutans* and *S. sobrinus* 6715 were exposed to 1 mM CAN, CAS or $AgNO_3$ in BHI growth media and allowed to grow 20 h (*See* Table 1) under similar conditions (no sucrose added) of the initial screening assay. Visible turbidity (+ +) was noticeable in all wells containing either 1 mM CAN or CAS after 20 h. In contrast, wells containing 1 mM $AgNO_3$ showed no visible signs (− −) of growth. The results demonstrate that both CAN and CAS do not inhibit *S. mutans* or *S. sobrinus* growth at 1 mM (Ce) in BHI, nearly *eight times* the concentration utilized in the initial screening assay.

2.6. Biofilm dispersal assay

Biofilm dispersal assays [21] were carried out to investigate if hydrolyzed Ce(IV) salts can disrupt the immature biofilm matrix produced by *S. mutans*. The use of 500 μM CAS as a dispersal agent resulted in a non-statistically significant reduction of adherent bacteria compared to the positive control. The dispersal assay was carried out with a CAS concentration *four times* that utilized in the initial screening assay described above. Non-targeted chemical disruption of the biomolecular components of the biofilm matrix by CAS as a mechanism of adherent cell reduction is unlikely, as a significant dispersal rate would have been achieved in this experiment. Instead, it is likely the hydrolyzed Ce (IV) salts target specific cellular events or biomolecules critical to the initial phases of biofilm formation.

Table 1
Planktonic cell viability assay with 1 mM metal ion.

BHI, 37 °C, 5% CO_2, 20 h	OD600	CAN	CAS	$AgNO_3$
S. mutans	0.010	+ +	+ +	− −
S. sobrinus	0.010	+ +	+ +	− −

2.7. Sucrose metabolism assay (acid production)

CeO_2-NP exhibit enzymatic activity based upon their surface oxidation state(s) and size in the media of interest [22]. Sucrose is both a building block for the synthesis of extracellular polysaccharides and an energy source for *S. mutans*. A sucrose metabolism assay was carried out similarly to reported methods [23] to test if the hydrolyzed Ce(IV) salts irreversibly modify sucrose in complex growth media so as to prevent its metabolism. Phenol Red Broth Base media was chosen both to limit media acidification due to the metabolism of other manufacturer added carbohydrates as well as to mimic the properties of BHI. At both 5 and 20 h incubation, a similar media acidification was observed (*See* Supplemental Data, Table S1) among the positive control and the Ce(IV) treated media. It is unlikely that the hydrolyzed Ce(IV) salts are irreversibly modifying sucrose to limit its metabolism in growth media.

2.8. Human cell proliferation assays

A human cell proliferation assay (24 h) was carried out testing the effects of hydrolyzed Ce(IV) salts and $AgNO_3$ (0–1 mM) on the metabolic activity of oral derived human cells, TIGK and HGF. $AgNO_3$ was used as the standard of clinical comparison, as it is utilized as a tooth-applied dental caries arresting agent. Similar metal ion concentrations of both CAN and CAS had less overall effect on the metabolic activity of TIGKs and HGFs as compared to $AgNO_3$. As shown in Fig. 4, treatment of both human cell populations with equimolar doses of $AgNO_3$ was consistent with statistically more cytotoxicity as compared to equivalent doses of hydrolyzed Ce(IV) salts CAN and CAS. It should be noted that intraoral application of Ag-containing agents are often applied at significantly higher concentrations than shown below.

2.9. Dynamic light scattering (DLS) studies

The hydrolysis of CAN or $[Ce(NO_3)_6]^{2-}$ yields an acidic solution with six equivalents of NO_3^- per one equivalent of Ce (*See* Eq. (1)). Raising the pH of CeO_2-NP obtained from Ce(IV) hydrolysis to remove adsorbed NO_3^- leads to aggregation and precipitation [17,19]. A 5 mM solution of $[Ce(NO_3)_6]^{2-}$ (or CAN) produces 30 mM NO_3^- upon hydrolysis, which must be accounted for in the DLS analysis. The commercially available CeO_2-NP screened for biological activity have zero (or limited) NO_3^- present in the dispersion. Thus, the commercially supplied CeO_2-NP dispersions were diluted to a concentration of 5 mM Ce and 30 mM KNO_3 to provide a consistent NO_3^- containing media for all species tested (*See* Supplemental Data, Fig. S2 A–E) with little change to the existing pH found upon simple dilution.

$$H_2[Ce(NO_3)_6] + 2H_2O \rightarrow CeO_2 + 6HNO_3 \quad (1)$$

Both CAN and $[Ce(NO_3)_6]^{2-}$ (30 mM NO_3^-) had average peak hydrodynamic diameters of approximately 9–10 nm (*See* Supplemental Data, Fig. S2 A–B). CeO_2-NP's prepared from Ce(IV) hydrolysis (*e.g.* $[Ce(NO_3)_6]^{2-}$) had a narrowed intensity distribution compared to commercially available CeO_2-NP of similar size (3 nm, Strem) in 30 mM KNO_3 (*See* Fig. 5). Fig. 6 illustrates the effect of a more strongly coordinating salt (40 mM KCl) on the hydrodynamic diameter and distribution of $[Ce(NO_3)_6]^{2-}$ *vs* CeO_2-NP (3 nm, Strem) in acidic media (*See* Fig. 6). At pH 7.4 (50 mM KH_2HPO_4) CeO_2-NP prepared from the hydrolysis of $[Ce(NO_3)_6]^{2-}$ aggregate to form a monodispersed distribution (Fig. 7) with limited stability over several h. Under the same pH conditions, CeO_2-NP (3 nm, Strem) fails to from an interpretable dispersion. It should be noted the average pH of the BHI (growth media) utilized in the cell based experiments is approximately 7.4.

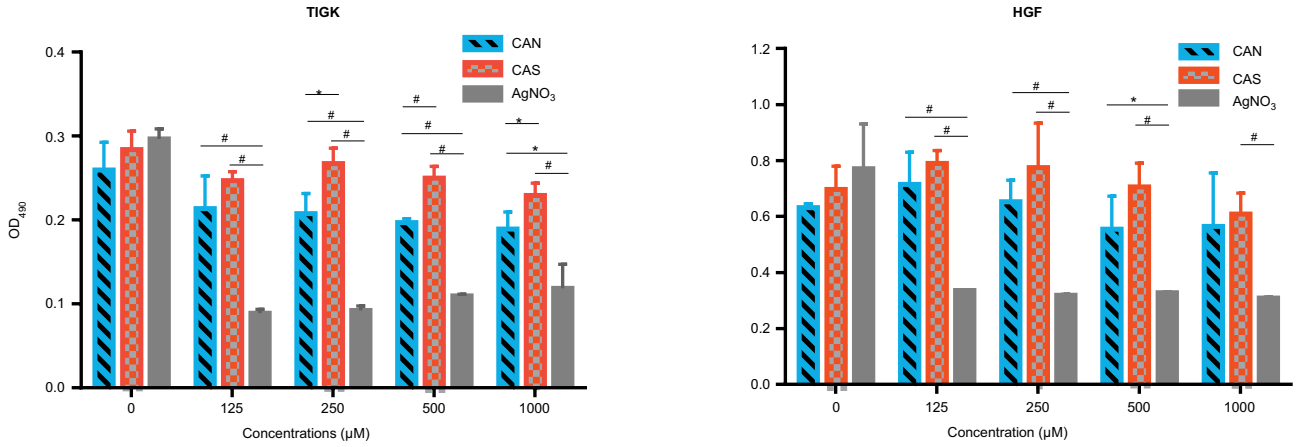

Fig. 4. MTS cell proliferation assays utilizing (left) TIGK and (right) HGF in the presence of hydrolyzed CAN (red), CAS (blue) and $AgNO_3$ (gray) for 24 h at 37 °C, 5% CO_2. $^{*}p < 0.05$, $^{\#}p < 0.01$, *t*-test. (For interpretation of the references to color in this figure legend, the reader is referred to the web version of this article.)

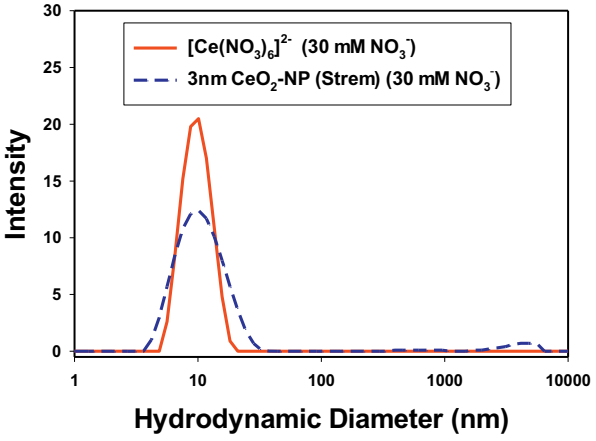

Fig. 5. Distribution of hydrolyzed $[Ce(NO_3)_6]^{2-}$ (pH 1.8) and CeO_2-NP (3 nm, Strem) (pH 4.5) in 30 mM NO_3^-.

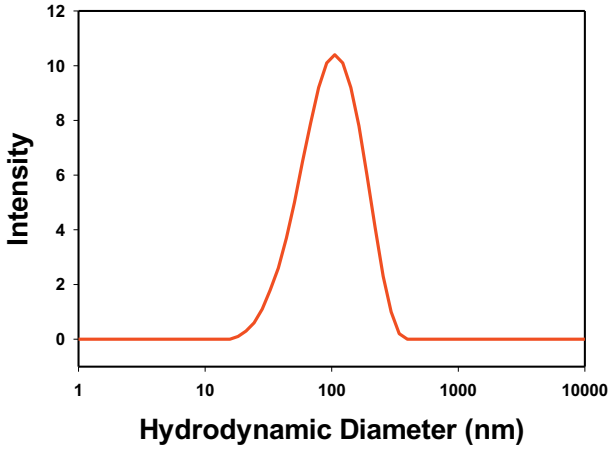

Fig. 7. Distribution of hydrolyzed $[Ce(NO_3)_6]^{2-}$ (500 μM Ce) in 50 mM KH_2PO4 (pH 7.4).

2.10. Scanning transmission electron microscopy (STEM) and electron energy-loss spectroscopy (EELS)

CeO_2-NP prepared by $[Ce(NO_3)_6]^{2-}$ hydrolysis and "bare" CeO_2-NP (3 nm, Strem) were encapsulated in graphene liquid cells [24] for STEM high-angle annular dark-field (HAADF) imaging and EELS analysis. The low-magnification HAADF images of hydrolyzed $[Ce(NO_3)_6]^{2-}$ and CeO_2-NP (3 nm, Strem) are shown as inserts in Fig. 8a–b, respectively. We find that compared with CeO_2-NP (3 nm, Strem), CeO_2-NP prepared by $[Ce(NO_3)_6]^{2-}$ hydrolysis tend to aggregate more, even after the samples were diluted significantly during the sample preparation process. Atomic-resolution HAADF images of the aggregated CeO_2-NP are shown in Fig. 8a–b. The lattice fringes of the CeO_2 nanoparticles can be clearly seen, indicating that the CeO_2-NP are fully crystalline. We did not observe any amorphous surface layer in either sample tested. Detailed analysis of many HAADF images revealed that the particle size in both samples is 3.5 nm on average, with a very narrow particle size

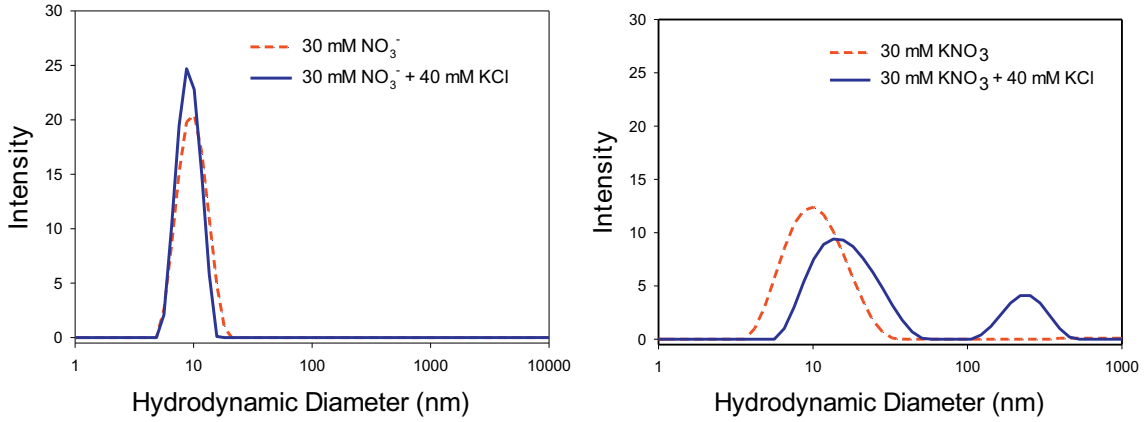

Fig. 6. Distribution of (left) 5 mM $[Ce(NO_3)_6]^{2-}$ (pH 1.8) and (right) 5 mM CeO_2-NP (3 nm, Strem) (pH 4.5) in 30 mM NO_3^- and with 40 mM KCl.

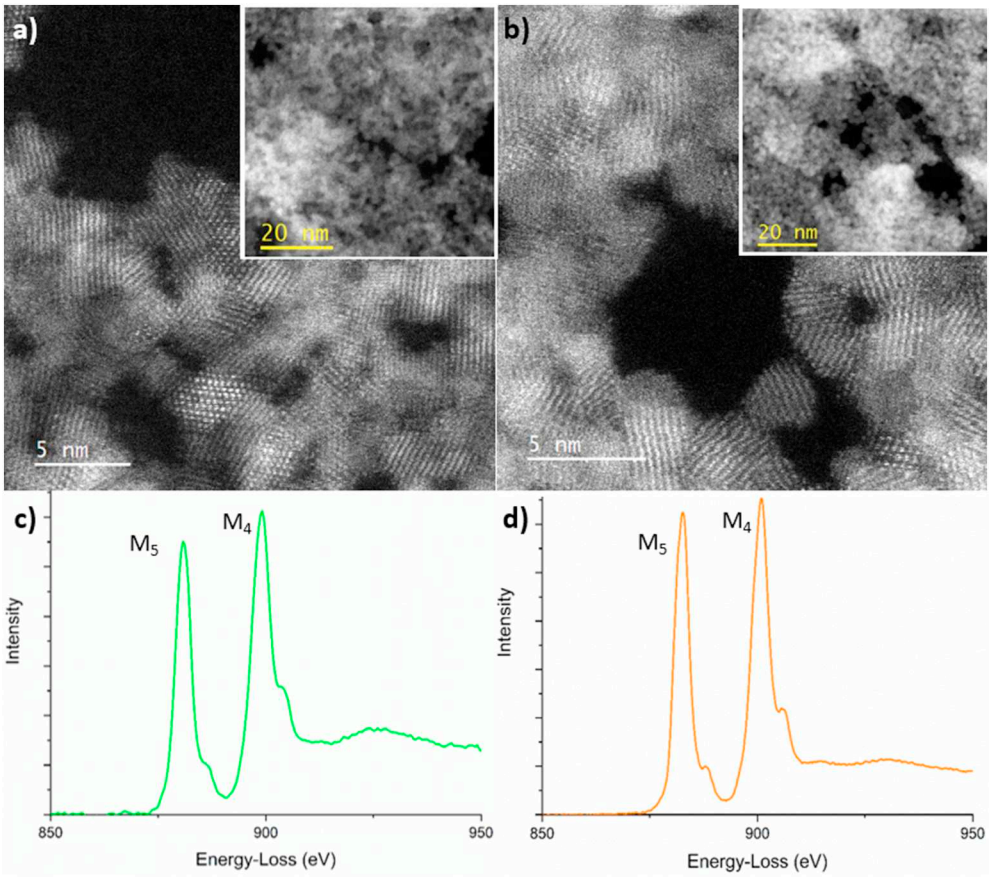

Fig. 8. Atomic-resolution high-angle annular dark field (HAADF) STEM images of (a) hydrolyzed $[Ce(NO_3)_6]^{2-}$ and (b) CeO_2-NP (3 nm, Strem) in graphene liquid cells. Inserts showlow magnification images of the nanoparticles. Electron energy-loss spectroscopy (EELS) of the Ce M-edges for (c) hydrolyzed $[Ce(NO_3)_6]^{2-}$ and (d) CeO_2-NP (3 nm, Strem) in graphene liquid cells, showing the M_4/M_5 ratio expected for a Ce (IV) valence state.

distribution. To confirm the oxidation state of aqueous dispersed CeO_2-NP, we performed EELS on CeO_2-NP encapsulated within the graphene liquid cells. Specifically, we have used the Ce *M*-edges to determine the Ce valence state. The Ce *M*-edge splits into two prominent peaks, the M_5 and the M_4 edges due to spin-orbit coupling of the initial states. Previous reports of Ce valence state analysis using EELS have found that the Ce M_5/M_4 ratio closely tracks with the Ce oxidation state, where the M_4 peak shows a higher intensity than the M_5 peak for Ce(IV), while the M_4 peak is lower in intensity than the M_5 peak in Ce(III) [24,25]. The Ce *M*-edge spectra for both samples are shown in Fig. 8c) and d) showing a higher intensity of the M_4 peak, corresponding to a Ce(IV) (*i.e.* fully stoichiometric CeO_2). We need to point out that for CeO_2-NP not dispersed in solution, but rather exposed to the vacuum of the transmission electron microscopy (TEM) column, we find that the valence state is reduced to Ce(III), as expected for particles with an average size of 3.5 nm [25].

2.11. CeO_2-NP surface properties and biological activity

The most suitable comparison between CeO_2-NP utilized in this study is between hydrolyzed $[Ce(NO_3)_6]^{2-}$ and CeO_2-NP (3 nm, Strem) due to the equivalent size (avg 3.5 nm), predominately Ce(IV) oxidation state and absence of ammonium ions. Hydrolyzed $[Ce(NO_3)_6]^{2-}$ are *more* stable at both higher ionic strength and as an aggregate at pH 7.4 compared to CeO_2-NP (3 nm, Strem). This underscores the idea that differential surface reactivity and aggregation properties exists between the two species of CeO_2-NP. This is brought about by the different synthetic methodology, specifically, the hydrolysis of a high valent Lewis acid yielding strongly acidic media, excess absorbable anions and a high surface area. [17]. It is likely the enhanced *in vitro* biofilm inhibiting capacity observed with hydrolyzed Ce(IV) salts reflects their differential surface reactivity and/or stability towards the biomolecular components of the growth media. This includes the potential for variable release and/or reduction of Ce(IV) ions on the CeO_2-NP surface [10]. It has been previously observed that the protein (or biomolecular) corona on the surface of metal oxide NPs has a significant influence on the resultant biological activity [26,27]. In the present study, it was found that rigorous mixing of hydrolyzed Ce(IV) salts in the growth media prior to initiation of adherent bacteria assays reduced their inhibitory activity - supporting a significant role of both surface reactivity and the protein corona on the observed biological activity. This study sets forth that the mechanism(s) of biofilm inhibition by hydrolyzed Ce (IV) salts is/are non-bactericidal at the concentrations tested. Further, the mechanism of biofilm inhibition is not consistent with irreversible reactivity of CeO_2-NP toward sucrose or non-targeted chemical disruption of the macromolecular components of the extracellular matrix as the predominate mode of biofilm inhibition. Current studies are underway to investigate not only the chemical reactivity with biological media components but also a relevant biological mechanism of activity.

3. Conclusions

CeO_2-NP of variable size and synthetic methodology were screened for the *in vitro* reduction of adherent *S. mutans* biofilm formation in complex growth media. While commercially available "bare" CeO_2-NP were ineffective at reducing adherent cells at the concentrations tested, hydrolyzed Ce(IV) salts prepared in strongly acidic media were active as *in vitro* biofilm inhibitors (IC_{50} = 137 μM). The inhibition likely takes place in the initial phases of biofilm formation utilizing one or multiple non-bactericidal mechanisms. Differences in biofilm inhibition between hydrolyzed Ce(IV) salts and commercially prepared CeO_2-NP of similar size (3.5 nm), distribution and oxidation state [Ce(IV)] are not attributed solely to the solution acidity, exogenous ions present (*e.g.*, NH_4^+, $NO3^-$, *etc.*) nor cytotoxicity. Further mechanistic studies

are underway focusing on both the chemical and biological aspects of biofilm inhibition of *S. mutans* and related species.

4. Materials and methods

All chemical reagents were purchased commercially and utilized without further purification. Ultrapure Milli-Q® water was used to prepare all samples for Dynamic Light Scattering (DLS), TEM data collection and UV–Vis Spectroscopy. Ceric ammonium nitrate hexahydrate (99.9%) (CAN) was purchased from Sigma-Aldrich, ceric ammonium sulfate dihydrate (98%) (CAS) was purchased from Acros and Ce$(NO_3)_3{\cdot}6H_2O$ (99.5%) was purchased from Alfa Aesar. Ceric nitrate (1.0 N aqueous solution) was purchased from GFS Chemicals (Columbus, Ohio). Commercially available "bare" cerium oxide nanoparticles (CeO_2-NP) were purchased and stored as the following colloidal dispersions: (1) Strem Chemicals (Newbury MA), 3 nm diameter CeO_2-NP, stored as an acidic dispersion at pH 3.5 ± 0.75, (2) Alfa Aesar (Ward Hill, MA) 10–20 nm diameter CeO_2-NP (20%), stored as an acidic dispersion at pH 1.5 with 0.2 mol NO_3^- per mole CeO_2-NP, and (3) Alfa Aesar, 30 nm diameter CeO_2-NP (15%). $AgNO_3$ and NH_4NO_3 were purchased from Ward's Science and KNO_3, KCl and $(NH_4)_2SO_4$ were purchased from Fisher Scientific. Disposable BrandTech PMMA cuvettes (Cole-Parmer, Vernon Hills, IL) were used for DLS measurements. Bacterial cultures were prepared from frozen glycerol stocks of *Streptococcus mutans* (UA159) or *Streptococcus sobrinus* (6715) in either sterilized Brain Heart Infusion (BHI) growth media (Criterion) or Phenol Red Broth Base (Sigma-Aldrich). All pH measurements were carried out on a Mettler Toledo FE20 benchtop pH meter following acidic and neutral pH calibration.

4.1. Hydrolysis/dilution of Ce(IV) salts

CeO_2-NP from Ceric Ammonium Nitrate. Following a similar preparation reported by Pettinger et al. [19], ceric ammonium nitrate hexahydrate (Aldrich, 13.7 mg) (CAN) was dissolved in 5.0 mL of deionized water at room temperature (rt) with gentle mixing for 20 s to afford a 5 mM (Ce) stock solution. The faint-orange colored solution faded within min to yield a clear dispersion. The UV–Vis absorption spectrum of CAN (NanoDrop™ 2000/2000c, Thermo Fisher) in H_2O (150 μM Ce) was in agreement with the literature, with a well-defined shoulder peak at 290 nm that intensifies significantly upon standing in solution over several h and an intense peak at approximately 230 nm is attributed to the absorption of NO_3^- [19]. (*See* Supplemental Data, Fig. S3).

CeO_2-NP from Ceric Ammonium Sulfate. A 5 mM (Ce) stock solution of ceric ammonium sulfate dihydrate (CAS) was prepared by dissolving CAS (15.8 mg) in 5.0 mL of deionized (DI) water at rt with gentle mixing for 20 s to produce an acidic dispersion of CeO_2-NP. The yellow tinted color faded within s to produce a clear dispersion. The UV–Vis absorption spectrum of CAS in H_2O (150 μM Ce) lacked a well-defined peak at 290 nm (and 230 nm) previously observed with CAN. Instead, a broadened peak with an absorption maximum at 275 nm was observed. (*See* Supplemental Data, Fig. S3).

CeO_2-NP from Ceric Nitrate. A 5 mM (Ce) stock solution of ceric nitrate ($H_2[Ce(NO_3)_6]$) was prepared by diluting a 1.0 N solution of $H_2[Ce(NO_3)_6]$ (25 μL) to 5.0 mL with 4.975 mL of DI water at rt with gentle mixing to produce an acidic dispersion of CeO_2-NP [17]. The deep yellow color faded over several min to produce a clear, acidic dispersion of CeO_2-NP.

4.2. Dynamic light scattering (DLS)

All size *vs* intensity data was collected at the UIC Nanotechnology Core Facility (NCF) utilizing a Malvern Zetasizer ZSP. The hydrodynamic diameter of each Ce-containing sample was collected as a function of intensity weighted distribution in a 30 mM NO_3^- buffer prepared in Milli-Q® water (18.2 MΩ). CAN and $H_2[Ce(NO_3)_6]$ were dissolved in Milli-Q® water to yield solutions containing 5 mM Ce and 30 mM NO_3^-. Commercially "bare" dispersions of CeO_2-NP were diluted with 30 mM KNO_3 solutions. This step was carried out to provide a consistent level of NO_3^- in each Ce-containing sample for DLS analysis. Both CAN and $H_2[Ce(NO_3)_6]$ yield six moles of NO_3^- present per each mole of Ce(IV) present, while commercially available, "bare" CeO_2-NP (Strem, Alfa Aesar) have zero (or small amounts of) NO_3^- present. Following standing at rt for 30–40 min, each Ce-containing sample was then vortexed for 2 min before being transferred into a polymethylmethacrylate (PMMA) disposable cuvette for an initial analysis (Supplemental Data, Fig. S2A–E). Additionally, a solution of KCl was added to stock solutions of $H_2[Ce(NO_3)_6]$ and CeO_2-NP (3 nm, Strem) in 30 mM NO_3^- to afford a higher ionic strength buffer with a stronger coordinating ligand (Cl^-) (Fig. 6). All size measurements were carried out with a minimum of 12 replicates and reported as an average intensity weighted distribution utilizing a 633 nm laser and a backscattering angle of 173°.

4.3. High resolution transmission electron microscopy (HR-TEM), STEM and EELS

HR-TEM images were recorded by a JEOL JEM-3010 microscope (operating at 300 kV) equipped with a Gatan Orius CCD camera for imaging and a Thermal-Noran XEDS detector. Solutions of CAN and CAS (5 mM) were dissolved in Ultrapure Milli-Q water, vortexed gently and allowed to stand approximately 20 h at rt prior to recording images. Dispersions were then further diluted 5-fold and to a concentration of approximately 1 mM Ce and pipetted (3–5 μL) onto a 400 Cu square mesh holey carbon TEM grid [21,22]. Excess water from the grid was wicked away and then dried in a vacuum desiccator for a minimum of 30 min prior to HR-TEM image collection (*See* Supplemental Data, Figs. S4–S5). The atomic resolution Z-contrast images and EELS maps were collected using the JEOL ARM200CF aberration corrected STEM with a cold-field emission gun operated at an acceleration voltage of 80 kV. The HAADF images were acquired using an annular dark-field detector with a collection angle ranging from 90 to 175 mrad. The probe convergence semi-angle was set to 29 mrad, which yields a probe size of 1 Å at 80 kV and a probe current of 62 pA. EELS characterization was conducted using the post-column Gatan Continuum GIF spectrometers. Samples were encapsulated in graphene liquid cells with aqueous media as previously reported [28–31]. $H_2[Ce(NO_3)_6]$ and CeO_2-NP (3 nm, Strem) samples were diluted to 5 mM (Ce) in Ultrapure Milli-Q water and stored at cold temperature prior to encapsulation.

4.4. In vitro adherent bacteria assay

An overnight culture of *S. mutans* UA159 was diluted and grown to mid exponential growth phase (OD600 = 0.5–0.6) in BHIgrowth media. The cells were diluted 40-fold into a BHI/1% sucrose solution and transferred to a 96-well, tissue cultured, PS microtiter plate. The wells of the microtiter plate were inoculated with freshly diluted BHI containing *S. mutans* and 1% sucrose and each appropriate stock solution to afford either 125 μM Ce containing agents or 1 mM NH_4NO_3/$(NH_4)_2SO_4$ to a total volume of 200 μL in each well. All stock solutions were prepared (hydrolyzed or diluted) within 30 min of addition to each microtiter plate. The wells were mixed gently with a microchannel pipette following addition of each agent. Both experimental and control wells were set up with six replicates. The microtiter plate was then placed in an incubator under the following conditions: 37 °C, 5% CO_2 for 20 h in the absence of light. Following the 20 h incubation time, the plates were gently submerged in a water bath 3–4 times to remove excess non-adherent cells and cellular debris. Each well was then stained with 200 μL of 0.1% crystal violet (CV) stain for approximately 30 min at 37 °C. The microtiter plate was then gently re-submerged (washed) in a deionized water bath, to remove excess dye and dry for a

minimum of 24 h. The dyed contents of each well were re-dissolved in 33% acetic acid with repeated mixing and diluted with DI water. The absorbance of each well at 570 nm (ABS570) was then recorded with a Victor3v plate reader, and the average absorbance of the six replicates were recorded. The ratio of the adherent bacteria present in the test wells *vs.* the positive control was determined by Eq. (2) and plotted in Fig. 1 as the mean ± SD. Note negative control absorbances at 570 nm were subtracted from each positive control and test well value.

$$\text{Adherent Bacteria Ratio} = [(ABS570_{\text{test well}})/(ABS570_{+\text{control}})] \quad (2)$$

4.5. Fluorescence microscopy of adherent biofilm

Lab-Tek® Chamber slide (8-well Permacol® Slide) was inoculated with *S. mutans* (BHI, 1% sucrose) in a manner similar as described above. The wells were run in duplicate, incorporating positive and negative controls, as well as 125 μM and 250 μM CAS treated wells at a volume of 400 μL. After 20 h of incubation at 37 °C, 5% CO_2, the chamber slide was rinsed gently with sterilized, deionized water to remove nonadherent cellular debris. Each well was then stained with 400 μL FilmTracer ™ SYPRO® Ruby Biofilm matrix stain according to the manufacturer's protocol. The chamber slide was then rinsed gently, and the chamber components were removed to allow visualization of the microscopic slide. 30 μL of sterilized water was added to each well and then a coverslip was placed. The slide was then viewed under a Nikon Eclipse E600 microscope at 10× magnification utilizing a TRITC emission filter.

4.6. Dose dependent reduction in adherent bacteria (IC_{50} determination)

The same protocol for culturing *S. mutans* UA159, dilutions and inoculation of a 96-well microtiter PS plate was followed as described above. A 5 mM stock solution of CAN was freshly prepared within 30 min of addition to the PS plate. The final volume of each well (test and controls) was 200 μL. Both test wells and controls were run with six replicates. The loaded microtiter plate was placed in an incubator at 37 °C, 5% CO_2 for 20 h in the absence of light. The same workup described above for removing non-adherent cells/debris, staining with 0.1% CV, quantification of retained CV stain on the Victor3v plate (ABS570) was followed. The adherent bacteria reduction was determined by Eq. (3) and plotted in Fig. S1 as the mean ± SD. The positive control was taken as the zero value for adherent bacteria reduction. Note negative control absorbances at 570 nm were subtracted from each positive control and test well value.

$$\text{Adherent Bacteria Reduction} = [(ABS570_{+\text{control}} - ABS570_{\text{test well}})/(ABS570_{+\text{control}})] \quad (3)$$

4.7. Bacterial cell viability assay

A similar protocol for overnight culturing of *S. mutans* UA159 was also employed for *S. sobrinus* 6715. Each culture was separately grown to mid log phase and diluted 40-fold similarly to above (the initial OD600 is reported in Table I). *S. mutans* and *S. sobrinus* and were then exposed to 1 mM CAN, CAS or $AgNO_3$ from pre-dissolved 5 mM (metal ion) solutions and diluted accordingly into a 24 well PS plate. The plate was allowed to stand for 20 h at 37 °C, 5% CO_2. Well turbidity was judged visually and designated with a positive sign (++).

4.8. Sucrose metabolism assay

A similar protocol for culturing of *S. mutans* UA159 in BHI and growing to mid log phase was followed as described earlier. A 4 mL culture was centrifuged down to a pellet at 4000*g* (10 min). To the pellet was added 4 mL of PBS solution, vortexed for 30 s, and re-centrifuged for 10 min (4000*g*). The wash cycle was repeated 3× to rid the sample of additional carbohydrates from BHI. Following the washing steps, the cell pellet was re-suspended in PBS to a final OD600 of 0.4. To 45 mL of sterilized Phenol Red Broth Base media was added a portion of the above PBS stock culture of *S. mutans* (40 fold dilution). Each autoclaved borosilicate glass tube (13 × 100 mm) was loaded with 2.85 mL of Phenol Red Broth Base media (with or without 1% sucrose), 0.150 mL CAN, 0.150 mL CAS or 0.150 mL of DI water for the positive control to total a 5.0 mL solutions in each tube. The media was allowed to grow for 20 h at 37 °C and 5% CO_2. Media acidity measurements were taken at 5 and 20 h. At each measurement, 1 mL of media broth was removed, diluted with 1 mL of DI water and the pH was recorded with a Mettler Toledo FE20 benchtop pH meter. The average pH of the triplicate measurement are reported in Table S1 (*See* Supplemental Data).

4.9. Biofilm dispersal assay

The same protocol for culturing *S. mutans* UA159, dilution(s) and inoculation of a 96-well microtiter PS plate was followed as described above. The positive control and test wells were prepared with a final volume of 200 μL (BHI + cells) and the negative control was prepared with only 200 μL BHI. The loaded microtiter plate was placed in an incubator at 37 °C, 5% CO_2 for 6 h in the absence of light. After 6 h, the planktonic cells were removed, the adherent biofilm rinsed (0.9% NaCl) and replaced with fresh 200 μL BHI (controls) or BHI/500 μM CAS (test wells). The same workup described above was used for removing non-adherent cells/debris, staining with 0.1% CV, quantification of retained CV on the Victor3v plate reader (ABS570) and calculation of adherent bacteria reduction (Eq. (3)). Note negative control absorbances at 570 nm were subtracted from each positive control and test well value.

4.10. Bacterial cell growth curve

A similar protocol for culturing *S. mutans* UA159, dilution(s) and inoculation of a 96-well microtiter PS plate was followed as described above. Test agents included 500 μM CAN and CAS and all test wells, positive and negative controls were run in triplicate. The OD600 of each well was recorded every 30 min for 10 h on a Victor3v plate reader. The average OD600 for each of the three triplicate runs (with standard deviation) was reported.

4.11. Human cell proliferation assays

3000 human telomerase immortalized gingival keratinocytes (TIGK, ATCC, Manassas, VA)/well were seeded in a 96-well plate in a culture medium (DermaLife K Medium Complete Kit, Lifeline Cell Technology) without the use of antibiotics. Two hours later, 10 mM stock solutions of CAN, CAS and $AgNO_3$ filtered through a 0.450 μM filter were used to deliver concentrations ranging from 125 to 1000 μM in the wells containing the cells were incubated for further 24 h. Cells were cultured in an incubator at 37 °C in 5% CO_2 environment. Cells without the addition of metal ions was used as the baseline control. Each treatment condition had three replicates. A cell proliferation assay was performed using CellTiter 96® Aqueous Non-Radioactive Cell Proliferation Assay kit (Promega, Madison, WI) per manufacturer's instructions. OD490 was read using a spectrophotometer (SPECTRAmax Plus, Molecular Devices, San Jose, CA). A similar human cell proliferation assay utilizing the same metal containing solutions was carried out with primary human gingival fibroblasts (HGF, ATCC, Manassas, VA) cultured in a DMEM (ThermoFisher, Scientific, Catalog No. 11965) with 10% FBS.

5. Data analysis

DLS, planktonic growth and dose dependent adherent bacteria reduction curves (IC_{50}) were plotted on SigmaPlot (Systat Software Inc., San Jose, CA). All data utilizing bacteria were expressed as the

mean ± SD. The curve generated from the dose dependent adherent bacteria reduction assay was fit to the Hill equation (3-parameter) to arrive at the reported IC_{50} value. Adherent bacteria and human cell proliferation data are expressed as means ± SD and plotted on GraphPad (GraphPad Software Inc., San Diego, CA). The Student *t*-test (two way) analysis of all test substances were performed using GraphPad Prism software where p values < 0.05 were considered statistically significant.

Abbreviations

BHI	brain heart infusion
CAN	ceric ammonium nitrate
CAS	ceric ammonium sulfate
CeO_2-NP	cerium oxide nanoparticles
TIGK	human telomerase immortalized gingival keratinocytes
HGF	primary human gingival fibroblasts
PS	polystyrene

Declaration of competing interest

We report no conflicts of interest in relation to this study or the materials utilized.

Acknowledgements

We would like to thank the Electron Microscopy Service and the Nanotechnology Core Facility (Research Resources Center, UIC) for use of instrumentation required to complete this study and Dr. Michael Johnson (UIC), Dr. Michael Federle (UIC) and Dr. Jeffrey Banas (University of Iowa) for comments regarding the preparation of this manuscript. We would also like to thank Dr. Joanna Burdette (UIC) for allowing use of the Nikon Light Microscope and Dr. Luisa A. DiPietro (UIC) for allowing use of her laboratory for human cell toxicity studies. Further, we would like to thank Dr. Fengyuan Shi (UIC) for her assistance in collecting and interpreting HR-TEM images presented in this manuscript. Finally, we would also like to thank Dr. Michael Federle for providing frozen glycerol stocks of *S. mutans* UA159 and *S. sobrinus* 6715. This work was supported by NIH/NIDCR Grants T32 DE018381 and 1K08DE028009-01A1 as well as the UIC Chancellor's Research Initiative Fund. The acquisition of the UIC JEOL JEM-ARM200CF was supported by the NSF MRI-R^2 grant (No. DMR-0959470), and the acquisition of the Gatan Continuum spectrometer was supported by a grant from the National Science Foundation MRI Program (No. DMR-1626065).

Credit author statement

RPP - Conceptualization, original manuscript draft, carried out all bacteria based biological assays, synthetic preparations, DLS studies and the experimental setup of all reported data. LC and JS - carried out the human cell proliferation studies, data analysis and manuscript editing. RFK, LB and JG - carried out the STEM/EELS studies, data analysis and manuscript editing. All authors read and approved manuscript prior to submission.

Appendix A. Supplementary data

Supplementary data to this article can be found online at https://doi.org/10.1016/j.jinorgbio.2020.110997.

References

[1] F.E. Dewhirst, T. Chen, J. Izard, B.J. Paster, A.C. Tanner, W.H. Yu, A. Lakshmanan, W.G. Wade, J. Bacteriol. 192 (2010) 5002–5017.
[2] M.I. Klein, G. Hwang, P.H. Santos, O.H. Campanella, H. Koo, Front. Cell. Infect. Microbiol. 5 (2015) 10.
[3] J.A. Lemos, S.R. Palmer, L. Zeng, Z.T. Wen, J.K. Kajfasz, I.A. Freires, J. Abranches, L.J. Brady, Microbiol Spectr 7 (2019).
[4] I.J. Davis, H. Richards, P. Mullany, Oral Microbiol. Immunol. 20 (2005) 191–194.
[5] K. Mijnendonckx, N. Leys, J. Mahillon, S. Silver, R. Van Houdt, Biometals 26 (2013) 609–621.
[6] R.P. Allaker, K. Memarzadeh, Int. J. Antimicrob. Agents 43 (2014) 95–104.
[7] M. Hannig, C. Hannig, Nat. Nanotechnol. 5 (2010) 565–569.
[8] N. Thakur, P. Manna, J. Das, J Nanobiotechnology 17 (2019) 84.
[9] I.A.P. Farias, C.C.L. Dos Santos, F.C. Sampaio, Biomed. Res. Int. 2018 (2018) 1923606.
[10] Y. Xu, C. Wang, J. Hou, P. Wang, L. Miao, G. You, Bioresour. Technol. 265 (2018) 102–109.
[11] Y. Xu, C. Wang, J. Hou, P. Wang, L. Miao, G. You, B. Lv, Y. Yang, F. Zhang, Bioresour. Technol. 245 (2017) 573–580.
[12] J.R. Lawrence, A. Paule, G.D.W. Swerhone, J. Roy, A.A. Grigoryan, J.J. Dynes, S.M. Chekabab, D.R. Korber, Environ. Pollut. (2019) 113515.
[13] A. Garcia, L. Delgado, J.A. Tora, E. Casals, E. Gonzalez, V. Puntes, X. Font, J. Carrera, A. Sanchez, J. Hazard. Mater. 199–200 (2012) 64–72.
[14] M.M. Masadeh, G.A. Karasneh, M.A. Al-Akhras, B.A. Albiss, K.M. Aljarah, S.I. Al-Azzam, K.H. Alzoubi, Cytotechnology 67 (2015) 427–435.
[15] Y. Xu, C. Wang, J. Hou, P. Wang, G. You, L. Miao, Environ. Sci. Pollut. Res. Int. 25 (2018) 34765–34776.
[16] Y. Xu, C. Wang, J. Hou, P. Wang, G. You, L. Miao, Environ. Sci. Pollut. Res. Int. 26 (2019) 9293–9304.
[17] M. Nabavi, O. Spalla, B. Cabane, J Colloid Interf Sci 160 (1993) 459–471.
[18] J.X. Xu, G.S. Li, L.P. Li, Mater. Res. Bull. 43 (2008) 990–995.
[19] N.W. Pettinger, R.E. Williams, J. Chen, B. Kohler, Phys. Chem. Chem. Phys. 19 (2017) 3523–3531.
[20] A. Ikeda-Ohno, C. Hennig, S. Weiss, T. Yaita, G. Bernhard, Chemistry 19 (2013) 7348–7360.
[21] S.S. Garcia, M.S. Blackledge, S. Michalek, L. Su, T. Ptacek, P. Eipers, C. Morrow, E.J. Lefkowitz, C. Melander, H. Wu, J. Dent. Res. 96 (2017) 807–814.
[22] C. Walkey, S. Das, S. Seal, J. Erlichman, K. Heckman, L. Ghibelli, E. Traversa, J.F. McGinnis, W.T. Self, Environ Sci Nano 2 (2015) 33–53.
[23] M. Matsumoto, T. Minami, H. Sasaki, S. Sobue, S. Hamada, T. Ooshima, Caries Res. 33 (1999) 441–445.
[24] F.F. Xu, Y. Bando, J. Appl. Phys. 89 (2001) 5469–5472.
[25] L.J. Wu, H.J. Wiesmann, A.R. Moodenbaugh, R.F. Klie, Y.M. Zhu, D.O. Welch, M. Suenaga, Phys. Rev. B 69 (2004).
[26] J. Shannahan, Nanotechnol. Rev. 6 (2017) 345–353.
[27] D. Docter, D. Westmeier, M. Markiewicz, S. Stolte, S.K. Knauer, R.H. Stauber, Chem. Soc. Rev. 44 (2015) 6094–6121.
[28] J.R. Jokisaari, C. Wang, Q. Qiao, X. Hu, D.A. Reed, R. Bleher, X. Luan, R.F. Klie, T.G.H. Diekwisch, ACS Nano 13 (2019) 3151–3161.
[29] C. Wang, T. Shokuhfar, R.F. Klie, Adv. Mater. 28 (2016) 7716–7722.
[30] C. Wang, Q. Qiao, T. Shokuhfar, R.F. Klie, Adv. Mater. 26 (2014) 3410–3414.
[31] A.R. Ribeiro, A. Mukherjee, X. Hu, S. Shafien, R. Ghodsi, K. He, S. Gemini-Piperni, C. Wang, R.F. Klie, T. Shokuhfar, R. Shahbazian-Yassar, R. Borojevic, L.A. Rocha, J.M. Granjeiro, Nanoscale 9 (2017) 10684–10693.